AGU PUBLICATIONS

Water Resources Research

RESEARCH ARTICLE
10.1002/2015WR017966

# Insights into lateral marsh retreat mechanism through localized field measurements

**M. Bendoni[1], R. Mel[2], L. Solari[1], S. Lanzoni[2], S. Francalanci[1,3], and H. Oumeraci[4]**

[1]Department of Civil and Environmental Engineering, University of Florence, Florence, Italy, [2]Department of Civil and Environmental Engineering, University of Padua, Padua, Italy, [3]CERAFRI, Center of Research and Advanced Education for Hydrogeological Risk Prevention, Florence, Italy, [4]Leichtweiß-Institut for Hydraulic Engineering and Water Resources, TU-Braunschweig, Braunschweig, Germany

**Key Points:**
- Lateral erosion and wave height at a salt marsh from field measurements
- The toe of the bank is more erodible than the top, promoting mass failures
- A less erodible vegetated bank top may lead to relatively higher lateral retreat

**Correspondence to:**
M. Bendoni,
mbendoni@dicea.unifi.it

**Citation:**
Bendoni, M., R. Mel, L. Solari, S. Lanzoni, S. Francalanci, and H. Oumeraci (2016), Insights into lateral marsh retreat mechanism through localized field measurements, *Water Resour. Res.*, *52*, 1446–1464, doi:10.1002/2015WR017966.

Received 8 AUG 2015
Accepted 5 FEB 2016
Accepted article online 8 FEB 2016
Published online 28 FEB 2016



**Abstract** Deterioration of salt marshes may be due to several factors related to increased anthropic pressure, sea level rise, and erosive processes. While salt marshes can reach equilibrium in the vertical direction, adapting to sea level rise, they are inherently unstable in the horizontal direction. Marsh boundaries are characterized by scarps with bare sediment below the vegetated surface layer that can be easily removed by wave-induced erosion. In this work, we explore the different mechanisms involved in the erosion of marsh borders through the interpretation of field data. The analysis is based on a systematic field monitoring of a salt marsh in the Venice Lagoon subject to lateral erosion. Measurements included horizontal retreat of the scarp at various locations and wave height in front of the marsh during three storm surges. Continuous erosion and mass failures alternated during the observed period, leading to an average retreat up to 80 cm/yr. The data, collected roughly every month for 1.5 year, indicate that the linear relation that links the observed erosion rate to the impinging wave power exhibits a larger slope than that already estimated in literature on the basis of long-term surveys. Moreover, an increase in the gradient of erodibility is detected along the marsh scarp, due to the combined action of soil strengthening by vegetation on the marsh surface and the impact of wave breaking at the bank toe, which promote cantilever failures and increase the lateral erosion rate.

## 1. Introduction

Salt marshes are biogeomorphic features, typical of ecotone environments, which provide several ecosystem services to coastal population [*Barbier et al.*, 2011]. In many parts of the world, the extent of marsh areas is reducing due to increased anthropic pressure and sea level rise that enhance erosive processes [*Gedan et al.*, 2009]. Average horizontal erosion rates were estimated, for different observation periods, in the order of 1.2–2.2 m/yr in case of the Lagoon of Venice (Italy) [*Day et al.*, 1998], 0.4–3.0 m/yr for the Westerschelde (Netherlands) [*Van der Wal et al.*, 2008], 0.5–2.0 m/yr in the Virginia Coastal Reserve (Virginia, USA) [*McLoughlin et al.*, 2014], and up to 2.3 m/yr along the Savannah River (Georgia, USA) [*Houser*, 2010].

Marsh retreat has relevant implications on the protection of coastal environments. Indeed, these areas are becoming intensely exposed to the impact of low-frequency hydrometeorological events, such as coastal floods induced by storm surges and sea level rise [*Howes et al.*, 2010] or human induced impacts [*Silliman et al.*, 2012]. To counteract this trend, many countries such as Italy (Lagoon of Venice), UK (Blackwater Estuary), and U.S. (Mississippi Delta) are currently restoring marsh systems [*Seminara et al.*, 2011]. New marsh land can both increase tidal water storage and attenuate wind waves associated with storm surges along exposed coast lines [*Day et al.*, 2007; *Temmerman et al.*, 2013].

Salt marshes can reach equilibrium in the vertical direction, such as in response to sea level rise [*French*, 2006; *Kirwan et al.*, 2010], but they are inherently unstable in the horizontal direction [*Mariotti and Fagherazzi*, 2013; *Fagherazzi et al.*, 2013]. One of the main mechanisms promoting the reduction of marsh surface is the lateral retreat of the edges induced by the action of the impinging waves [*Schwimmer*, 2001; *Van der Wal et al.*, 2008; *Mariotti and Fagherazzi*, 2010; *Marani et al.*, 2011; *Leonardi and Fagherazzi*, 2014]. This mechanism is characterized by the alternation of continuous (particle by particle) erosion and occasional mass failures [*Van Eerdt*, 1985; *Francalanci et al.*, 2013; *Bendoni et al.*, 2014], and it is also controlled by the extent

of the tidal basin adjacent to the marsh edge, determining the offshore wave climate [*Mariotti and Fagherazzi*, 2013].

Relationships between wave energy flux and volumetric erosion rate were determined at different sites by *Schwimmer* [2001], *Marani et al*. [2011], and *McLoughlin et al*. [2014]. *Houser* [2010] investigated the effect of peak wave force on cumulative bank retreat, whereas *Ravens et al*. [2009] found that marsh area loss is mostly driven by low sediment supply instead of waves-induced erosion at a specific site. These analyses were based on field data collected over large spatial (kilometers) and temporal scales (decades), and provide an estimation of the overall evolution of the system. A more localized analysis was carried out by *Feagin et al*. [2009], who measured in the field the elevation changes of a vegetated and unvegetated marsh edge. They argued that vegetation plays a role on the erosion of the marsh boundaries by indirectly affecting the soil characteristics and it does not necessarily reduce the lateral erosion of wetland edges.

Nevertheless, such analyses do not allow to identify the relative contribution of the specific processes (e.g., continuous erosion and mass failures) and the possible intrinsic variability of the analyzed system (such as differences in soil composition or local bathymetry). In addition, wave energy flux striking the marsh edge was determined by means of mathematical models and no measurements of local wave climate have been carried out. Waves were instead measured close to the bank edge by other authors with different aims: to study the effect of marsh vegetation on wave energy dissipation [*Moller*, 1999, 2006; *Jadhav et al*., 2013], to distinguish the relative importance of waves and tidal flows on salt marsh developments [*Callaghan et al*., 2010], to characterize wave transformation inside a wave-cut gully [*Priestas and Fagherazzi*, 2011], or to distinguish the effect of wind waves and vessel-generated waves [*Houser*, 2010]. To our knowledge, no systematic wave height measurements specifically aimed at the study of erosive trends are available in literature. The lack of localized and continuous marsh erosion monitoring is a relevant limitation as there is an impelling need to develop and use physics-based tools for the prediction of lateral retreat of salt marshes.

*Leonardi and Fagherazzi* [2014], through an analysis of the statistical distribution of erosion events and a cellular automata model, highlighted the different behaviors between salt marshes exposed to strong and weak wave forcing. They argued the impossibility to clearly predict when failure events occur for low exposed marshes. However, they referred to yearly measurements of marsh edge position, thus suggesting that further insights can only be provided by more frequent field surveys.

In this work, we focus on the mechanisms involved in the lateral marsh retreat and on the definition and interpretation of physics-based relationships between the observed retreat rate and impinging wave power. The work is based on a field monitoring campaign on a retreating salt marsh in the Lagoon of Venice by means of systematic and frequent (about once a month) surveys on erosion pins, and detailed measurements of wave height close to the bank edge during three storm surges. Wave height data were used to calibrate an empirical model for local wave forecasting. Results allow one to quantify the relative importance of continuous erosion and mass failures on the total observed retreat.

The measured erosion rates were then expressed as a function of the incident wave power, showing differences with respect to previous formulations [*Marani et al*., 2011], possibly due to the different temporal scales characterizing the considered data sets.

The observed cumulative retreats were finally interpreted as a function of the variable scarp erodibility along the vertical direction, by means of a simple mathematical model where the scarp is composed by two layers subject to different erosion rates. Results suggest that the presence of vegetation on the marsh surface does not necessarily produce a positive feedback on the reduction of lateral retreat.

## 2. Surveyed Area and Erosive Trend

The salt marsh surveyed in the present study is located in the north part of the Lagoon of Venice, west of Sant'Erasmo island, 45°28′11″N, 12°23′41″E (Figure 1a). The area is characterized by a microtidal regime (tidal range in the order of 60 cm), a negligible external input of sediment, and salt marshes have bank heights in the range 0.3–0.8 m, from the top to the toe (Figures 1c and 2). Some portions of the marsh border are quite irregular and the borderline is exposed to north-east, north-west, and south-east directions, depending on the orientation of the banks. The margin is characterized by steep slope cliffs (Figures 1c and 2), covered by vegetation, some unvegetated gullies, with a gentler slope, and a few narrow incisions dissecting

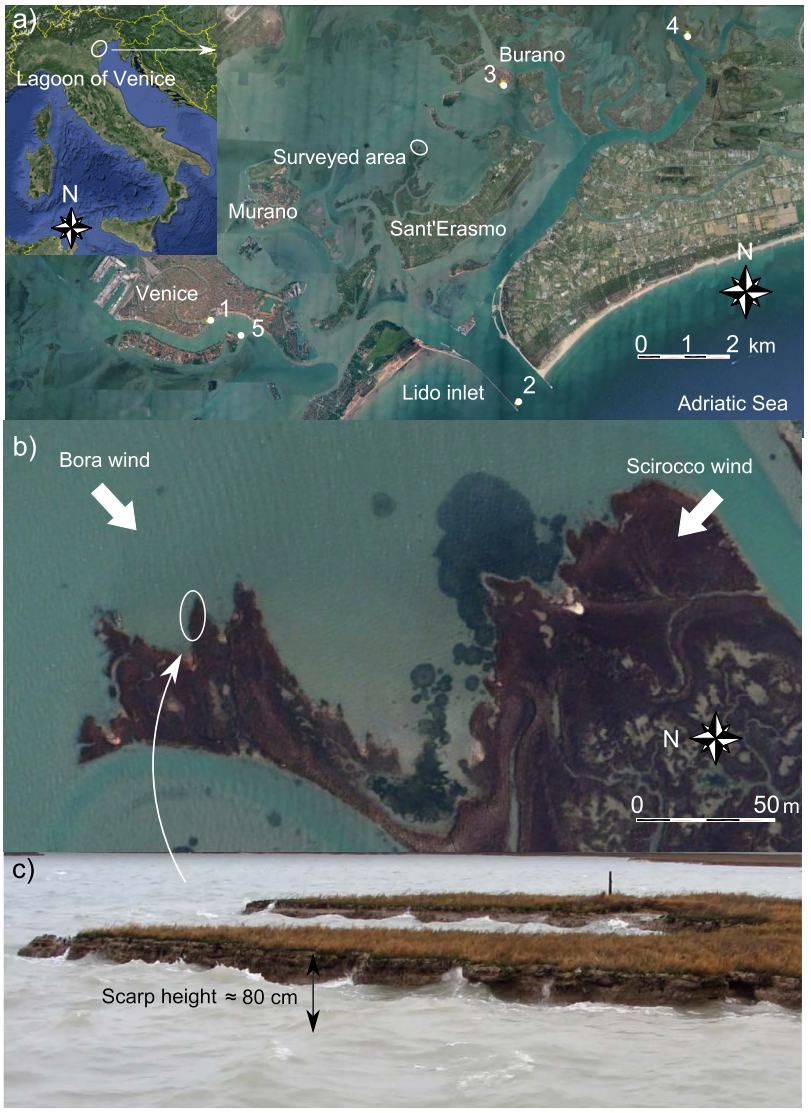


**Figure 1.** (a) Locations of the investigated salt marsh (encircled) and of the stations monitoring the tidal elevation, managed by the Tide Center of the Municipality of Venice: 1, Punta Salute; 2, Diga Sud Lido; 3, Burano; 4, Laguna Nord Saline; and 5, San Giorgio. (b) Enlarged view of the monitored marsh. Arrows indicate Bora and Scirocco wind directions. Circled area represents the salt marsh edge reported in Figure 1c. (c) View of the salt marsh border subject to wave forcing during November 2013.

the marsh and exhibiting a sharp slope variation between the marsh top and the adjacent mudflat. The top of the marsh (identified by GPS measurements) is about 25 cm above the mean sea level (MSL) that is, since 2009 to date, approximately 30 cm above the reference level of Punta Salute (PS). PS is used as zero reference for the water level measurements from the permanent monitoring stations managed by the Tidal Center of the Municipality of Venice (Web page URL: http://www.comune.venezia.it/flex/cm/pages/ServeBLOB.php/L/IT/IDPagina/1748).

North-east is the direction of the dominant "Bora" wind, quite frequent from October to late spring [*Poulain and Raicich*, 2007]. It can reach speeds up to 20 m/s and leads to the most adverse storm surges. "Scirocco" wind blowing from south-east dominates the summer season, but it usually does not exceed 5 m/s (Figure 1b). However, during summer, occasional short storm surges are characterized by north-west direction winds which can easily reach 15–20 m/s.

The marsh border has considerably retreated during the last 30 years, as documented in Figure 3, through the comparison of aerial photographs taken in 1978 and 2010. The top of the retreating scarp was identified

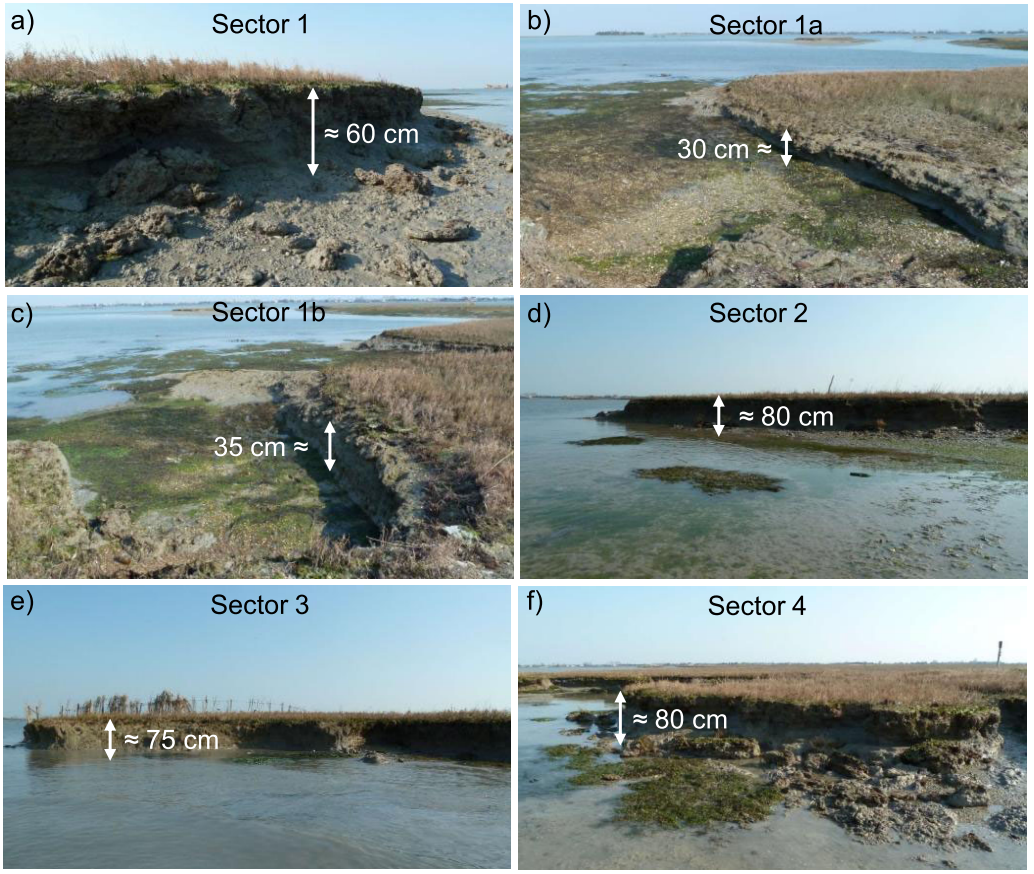


**Figure 2.** Views of the marsh edge at low tide in the surveyed sectors, with indicated local bank heights.

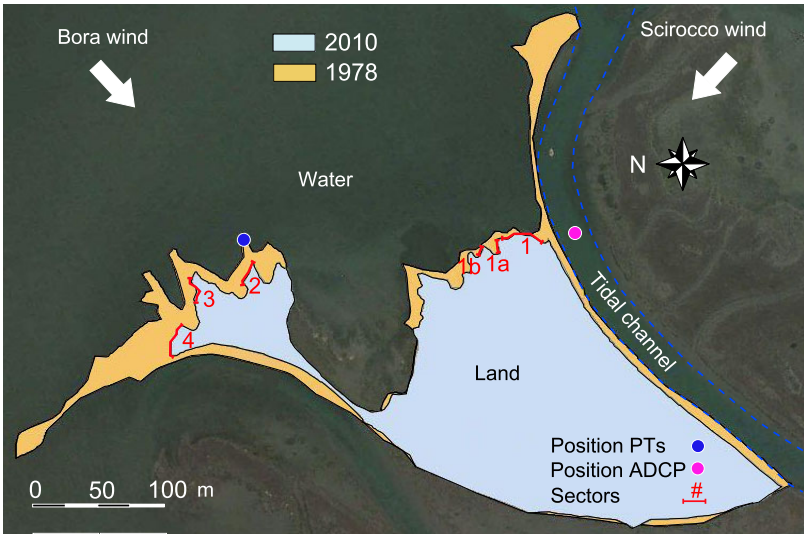


**Figure 3.** Observed retreat area estimated through comparison of aerial photographs collected in 1978 and 2010, available on the GeoPortale IDT provided by Regione Veneto (http://idt.regione.veneto.it/app/metacatalog/). Red lines denote the six marsh edge sectors where the erosion pins have been placed. A blue dot identifies the position of the pressure transducers used to measure the wave heights, while a magenta dot denotes the point where ADCP measurements of tidal currents were carried out. Blue dashed lines denote the tidal channel adjacent to the monitored marsh.

as the interface between vegetated and unvegetated areas (the vegetated front). The error, determined by the pixel size, is of the order of $\pm 1.0$ m.

Figure 3 shows that the marsh surface loss depends not only on the border orientation but also on the location within the marsh. This peculiar behavior is likely due to the coupled effect of wind waves and boat waves. Indeed, the northernmost marsh edge, associated with the highest erosion, is subject not only to wind waves originated by Bora winds and sporadic but intense north-west winds but also to waves generated at a distance of about 800–900 m by boats traveling from Venice and Murano to Burano. Conversely, the salt marsh banks facing east direction are adjacent to an area with a low boat traffic and, hence, can be directly affected only by Bora wind waves.

In order to characterize the various erosive patterns at time scales of months, we identified four different sectors (1–4), and two subsectors (1a and 1b) to be analyzed along the marsh borderline (Figures 2 and 3). They were recognized on the base of the different edge orientations and erosive trends. All sectors tend to be exposed to Bora wind. Sectors 1 and 2 are only partially affected by summer storm surges (coming from north-west) and are less exposed to possible boat waves. Sector 3, due to its orientation, is mainly reached by north-east waves almost parallel to the boundary, and it might show a different behavior with respect to other sectors. Sector 4 can be subject to both north-west and frequent north-east waves characterizing the winter storm surges. Sector 1 is the only one directly exposed to light Scirocco winds and it is of interest to verify if such weak forcing can also affect the erosive trend.

Figure 2 illustrates a view of the scarps characterizing each sector. The main retreat mechanism has been found to be the continuous erosion (i.e., removal of sediment particles or small lumps of soil), alternated to mass failures, mostly of cantilever type. The entity and frequency of mass failures change according to the sector. At the toe of the shortest edges (sectors 1a and 1b), we rarely observed collapsed blocks. This can be ascribed to the fact that cantilever profiles tend to develop more slowly, due to the lower height of the bank (Figures 2b and 2c) which is less prone to wave attack; moreover, slumped blocks are smaller and can be eroded by the flow more rapidly. Sectors with higher banks show blocks of different dimensions at the toe (Figures 2a, 2d, 2e, and 2f). In general, sector 4 is subject to more frequent and larger cantilever failures than the others, whereas sector 3, although close to it, is not regularly affected by this type of erosion events. Patches of pioneer vegetation are generally present on the mudflats adjacent to all sectors.

For each sector, the composition of the soil has been analyzed collecting three samples (A–C) at different location along the scarp of the salt marsh, at the top, at the toe, and at the beginning of the scarp (Figure 4, Table 1). The sand fraction in the top layer A is in the range 21–23.4%, while the lower layer has the largest clay content, varying in the range 32–37%. The layer C in front of the bank toe has the largest variability among the four sectors: sector 1 has the highest sand content; sectors 3 and 4 have the highest clay content.

As vegetation is concerned, a visual survey indicated that the vegetation cover mainly consisted of *Limonium narbonense* and *Salicornia* in all the monitored sectors. The patches of vegetation were irregularly spread over the marsh surface and, in some areas, more than one species was present. A summary of the observed plant cover in each of the sectors is reported in Table 2.

## 3. Setup and Methodologies

The aim of the present field measurement is to determine the relationship between wave forcing impinging on the marsh edge and local erosion rates. The wave height $H_{m0,M}$ measured by pressure gauges placed close to the marsh bank (inshore wave climate) was related to the wave height $H_{m0,E}$ characterizing the intertidal areas in front of the monitored marsh (offshore wave climate) through hourly data of wind, fetch, and water depth (Figure 5). The resulting relationship between $H_{m0,M}$ and $H_{m0,E}$ is used to estimate continuously the inshore forcing given offshore wave climate, thus avoiding a permanent deployment of instrumentation in the field.

Inshore wave climate $H_{m0,M}$ was measured for three storm events occurred on 18, 21, and 28 February 2014. Wind, fetch, and water depth data needed to estimate the offshore wave climate $H_{m0,E}$, were provided every hour by five permanent stations, located in the northern part of the Lagoon of Venice, close to the Lido inlet (Figure 1a).

Erosion rates were monitored since November 2013 and 17 surveys, identifying 16 different time intervals, were carried out till April 2015 (Table 3).

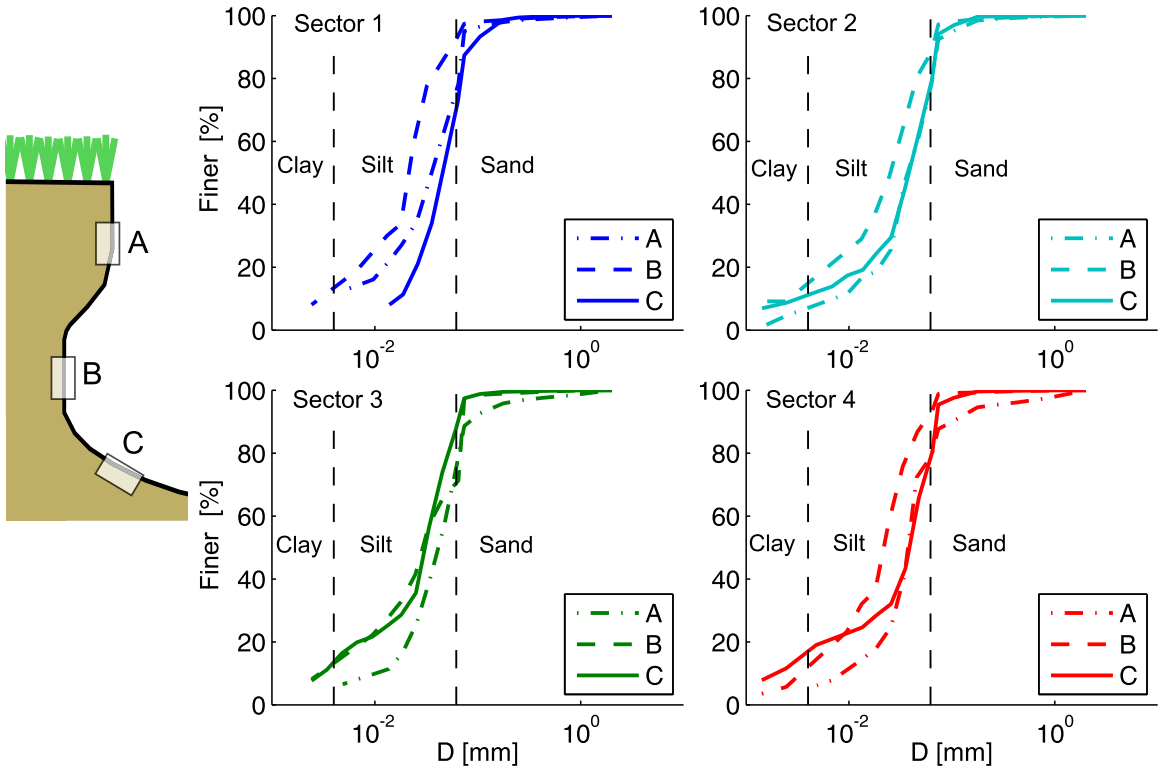


**Figure 4.** Soil composition characterizing the surveyed sectors. Soil samples are collected at different positions of the marsh scarp: A corresponds to the upper part, B to the lower part, and C to the area immediately adjacent to the bank toe. Clay: $D < 0.004$ mm; silt: $0.004 \leq D < 0.062$ mm; and sand: $D > 0.062$ mm.

### 3.1. Wave Climate From Pressure Gauges ($H_{m0,M}$)

Two pressure transducers (PTs) Series 46x, produced by Keller Instruments, were used to measure inshore wave climate. The transducers were calibrated in a laboratory tank, considering various water depths. Their resolution is 0.1 mbar (1 mm) and the range of measurement is 0.0–100.0 mbar (0.0–1.0 m). The sensors were located about 7–8 m from the scarp of the marsh edge (Figure 3), at a distance of 15 cm from the bottom of the tidal flat next to the marsh (Figure 5). The transducer membrane was arranged face down to prevent sediment settling on it and to avoid the dynamic pressure effect generated by the velocity component normal to the sensor face [*Cavaleri*, 1980]. Variations of the atmospheric pressure during storm surges are quite limited in the monitored area. For this reason, no atmospheric pressure correction was carried out on the collected data. Data were collected by a data logger located inside a waterproof caisson raised with respect to the marsh surface and secured to the ground. The sampling rate was set to 6 Hz; 17 min of recording (one burst) started every 1.5 h. Overall, a time period of roughly 87 h was monitored. Sampling rate, number of bursts, and duration were selected in order to find a balance between the needs to characterize the wave field and the storage capacity of the data logger. Table 4 provides a summary of the measurements.

**Table 1.** Soil Fractions for the Different Sectors and Different Positions Along the Bank Scarp

| | Sector 1 | Sector 2 | Sector 3 | Sector 4 |
|---|---|---|---|---|
| A | | | | |
| Sand | 21.7 | 21.7 | 23.4 | 20.9 |
| Silt | 51.2 | 59.7 | 60.3 | 61.1 |
| Clay | 27.1 | 18.6 | 16.3 | 18.0 |
| B | | | | |
| Sand | 7.6 | 11.5 | 28.7 | 6.7 |
| Silt | 58.7 | 51.6 | 38.6 | 57.0 |
| Clay | 33.7 | 36.9 | 32.7 | 36.3 |
| C | | | | |
| Sand | 27.2 | 20.1 | 12.1 | 19.4 |
| Silt | 61.4 | 55.6 | 59.3 | 52.2 |
| Clay | 11.4 | 24.3 | 28.6 | 28.4 |

We deployed the PTs on the tidal flat facing the monitored marsh (see Figure 3), where current velocities are likely low and, hence, the linear wave theory can be used to estimate wave climate [*Bishop and Donelan*, 1987; *Jones and Monismith*, 2007]. This is also in agreement with the recommendations of *Lee and Wang* [1984] and *Bird* [1993] for the measurement of wave climate both in intermediate and shallow water.

**Table 2.** Different Typologies of Vegetation Present on the Surveyed Sectors

| | Sector | | | |
|---|---|---|---|---|
| | 1 | 2 | 3 | 4 |
| *Aster tripolium* | | x | | |
| *Limbarda crithmoides* | | x | x | x |
| *Limonium narbonense* | x | x | x | x |
| *Puccinellia palustris* | | | x | x |
| *Salicornia* | x | x | x | x |
| *Suaeda maritima* | x | x | | |

The significant wave height we are interested in can be obtained from the relation $H_{m0,M}=4\sqrt{m_0}$ [*Dean and Darlymple*, 1991], where $m_0$ is the zero moment of the spectral density distribution of water surface displacement, $S_{\eta\eta}$. According to the linear wave theory, the relation between $S_{\eta\eta}$ and the spectral density distributions of pressure head, $S_{pp}$, leads to

$$S_{\eta\eta}(f)=\frac{1}{K_p^2}S_{pp}(f,h_p) \tag{1}$$

where $f$ is the angular frequency, and $h_p$ is the mean height of the water column above the PT located at a distance $d_p$ from the bed. The pressure response factor $K_p=\frac{\cosh(kd_p)}{\cosh[k(h_p+d_p)]}$ [*Dean and Darlymple*, 1991] is computed with respect to the wave number $k$, which, in turn, is determined from the dispersion relation $\omega^2=gk\tanh[k(h_p+d_p)]$, with $\omega$ the wave frequency and $g$ the acceleration of gravity.

The following procedure is carried out to obtain $S_{pp}(f,h_p)$ from the collected data. First, a 3-$\sigma$ filter using a five data points window is applied to rough data, averaged over the two PTs, to remove spikes. The erased information, resulting about 0.1–0.2% of the total amount of data, was replaced by a linear interpolation of the surrounding data points. Then, a spectral analysis on each filtered time series was carried out using the modified Welch method [*Welch*, 1967]. Each record was detrended and divided into segments of 128 data points, overlapping by 50% and Hamming windowed. Finally, a Fast Fourier Transform [*Cooley and Tukey*, 1965] algorithm was applied to each segment and the resulting spectra were averaged to obtain the pressure head density spectrum $S_{pp}(f,h_p)$ representative of each burst.

The determination of the spectral density $S_{\eta\eta}(f)$ from $S_{pp}(f,h_p)$, through equation (1), is not straightforward, as $K_p$ tends to reach too high values with increasing wave frequency and submergence of the sensor. In order to obtain a reliable estimation of $S_{\eta\eta}(f)$, we applied equation (1) in the interval $f\in[0,f_c]$ and approximated the tail of the spectrum as $f^{-5}$ [*Wolf*, 1997]. The cutoff frequency, $f_c$ was chosen as the minimum value among those proposed in literature to avoid overestimation of the wave height, namely [*Tucker and Pitt*, 2001; *Jones and Monismith*, 2007]:

$$f_c=\min\begin{cases} f_c|K_p^2(f_c)=0.01 & [\textit{Tucker and Pitt},\ 2001] \\ f_c\left|\frac{S_{pp}(f_c)}{W_n}=a_1\right. & [\textit{Jones and Monismith},\ 2007] \\ a_2\cdot f_p & [\textit{Jones and Monismith},\ 2007] \\ f_T \end{cases} \tag{2}$$

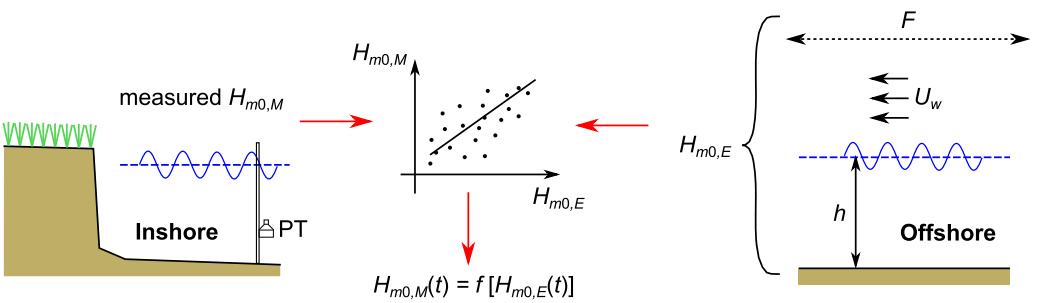


**Figure 5.** Sketch representing the procedure employed to estimate wave forcing at the marsh scarp. A functional relation is determined between the zeroth moment wave height measured inshore, $H_{m0,M}$ and $H_{m0,E}$ estimated through equation (4) (on the basis of offshore wind velocities and water depths provided by the monitoring stations shown in Figure 1). PT: pressure transducer, $F$: fetch, $U_w$: wind velocity, and $h$: offshore water depth.

**Table 3.** Summary of the Field Surveys Carried Out in the Monitored Marsh[a]

| Nr. | $\Delta T$ (Days) | Dates |
|---|---|---|
| 1 | | 29 Nov 2013 |
| 2 | 81 | 18 Feb 2014 |
| 3 | 10 | 1 Mar 2014 |
| 4 | 6 | 7 Mar 2014 |
| 5 | 54 | 30 Apr 2014 |
| 6 | 27 | 27 May 2014 |
| 7 | 29 | 24 Jun 2014 |
| 8 | 27 | 21 Jul 2014 |
| 9 | 29 | 19 Aug 2014 |
| 10 | 30 | 18 Sep 2014 |
| 11 | 30 | 19 Oct 2014 |
| 12 | 39 | 27 Nov 2014 |
| 13 | 21 | 18 Dec 2015 |
| 14 | 33 | 21 Jan 2015 |
| 15 | 31 | 21 Feb 2015 |
| 16 | 26 | 19 Mar 2015 |
| 17 | 28 | 15 Apr 2015 |

[a]The first column reports the ordering number; the second column reports the time interval elapsed between two consecutive surveys; and the third column reports the dates of the surveys.

The noise floor of the instrument $W_n$, was computed as $Res=\sqrt{\frac{f_s W_n}{2}}$, with $f_s$ the sampling frequency and $Res$ the resolution of the pressure gauge. The constants $a_1$ and $a_2$ have been set equal to 12 and 1.1, respectively [*Jones and Monismith*, 2007] and $f_p$ is the peak frequency of the pressure head density spectrum. $f_T$ represents the highest frequency at which the pressure fluctuation induced by a traveling wave can be detected at a distance $h_p$ from the mean free surface, determined through linear dispersion relation:

$$f_T=\frac{1}{2\pi}\sqrt{g\frac{\pi}{h_p}\tanh\left[\frac{\pi(h_p+d_p)}{h_p}\right]} \tag{3}$$

### 3.2. Wave Climate From Wind, Fetch, and Depth Data ($H_{m0,E}$)

The offshore wave climate was determined using the wave forecast model proposed by *Young and Verhagen* [1996] and further improved by *Breugem and Holthuijsen* [2007]. This model was specifically developed to estimate the wave height for a not fully developed sea in shallow water environments with limited fetches. The relationships employed to obtain significant wave height $H_{m0,E}$ and the peak period $T_p$ are

$$\frac{gH_{m0,E}}{U_w^2}=0.240\left\{\tanh A_1\tanh\left[\frac{B_1}{\tanh A_1}\right]\right\}^{0.572} \tag{4}$$

$$\frac{gT_p}{U_w}=7.690\left\{\tanh A_2\tanh\left[\frac{B_2}{\tanh A_2}\right]\right\}^{0.187} \tag{5}$$

where $A_1=0.343(gh/U_w^2)^{1.14}$, $B_1=4.41\cdot10^{-4}(gF/U_w^2)^{0.79}$, $A_2=0.10(gh/U_w^2)^{2.01}$, $B_2=2.77\cdot10^{-7}(gF/U_w^2)^{1.45}$. Here $h$, $U_w$, and $F(\theta_w)$ are the average water depth, the wind speed offshore the considered marsh, and the corresponding fetch length, respectively.

Since the morphology of the investigated area is quite irregular, we determined the values of effective fetches to be employed in the calculation, through the relation proposed by Saville [1954]:

$$F(\theta_k)=\frac{\sum_{s=-45}^{45}F(\theta_{k+s})\cos^2\left(s\frac{\pi}{180}\right)}{\sum_{s=-45}^{45}\cos\left(s\frac{\pi}{180}\right)} \tag{6}$$

where $F(\theta_k)$ is the fetch length associated with the kth wind direction.

We then assumed that the direction of wave propagation adapts instantaneously to the wind direction $\theta_w(t)$ and, for each direction, we computed the space averaged bed elevation $z_b(\theta_w(t))$, and water depth $h(\theta_w(t))=\eta(t)-z_b(\theta_w(t))$, considering the hourly values of the water surface elevation $\eta(t)$ with respect to Punta della Salute.

**Table 4.** Summary of the Field Surveys Carried Out to Measure the Inshore Wave Climate in Front of the Marsh During Three Storm Surges

| Start Time | | End Time | | | |
|---|---|---|---|---|---|
| Date | Time | Date | Time | Duration (h) | Number of Bursts |
| 18 Feb 2014 | 6:00 P.M. | 20 Feb 2014 | 2:00 A.M. | 32 | 22 |
| 21 Feb 2014 | 4:30 P.M. | 22 Feb 2014 | 5:00 P.M. | 24.5 | 17 |
| 28 Feb 2014 | 4:30 P.M. | 1 Mar 2014 | 11:00 P.M. | 30.3 | 21 |

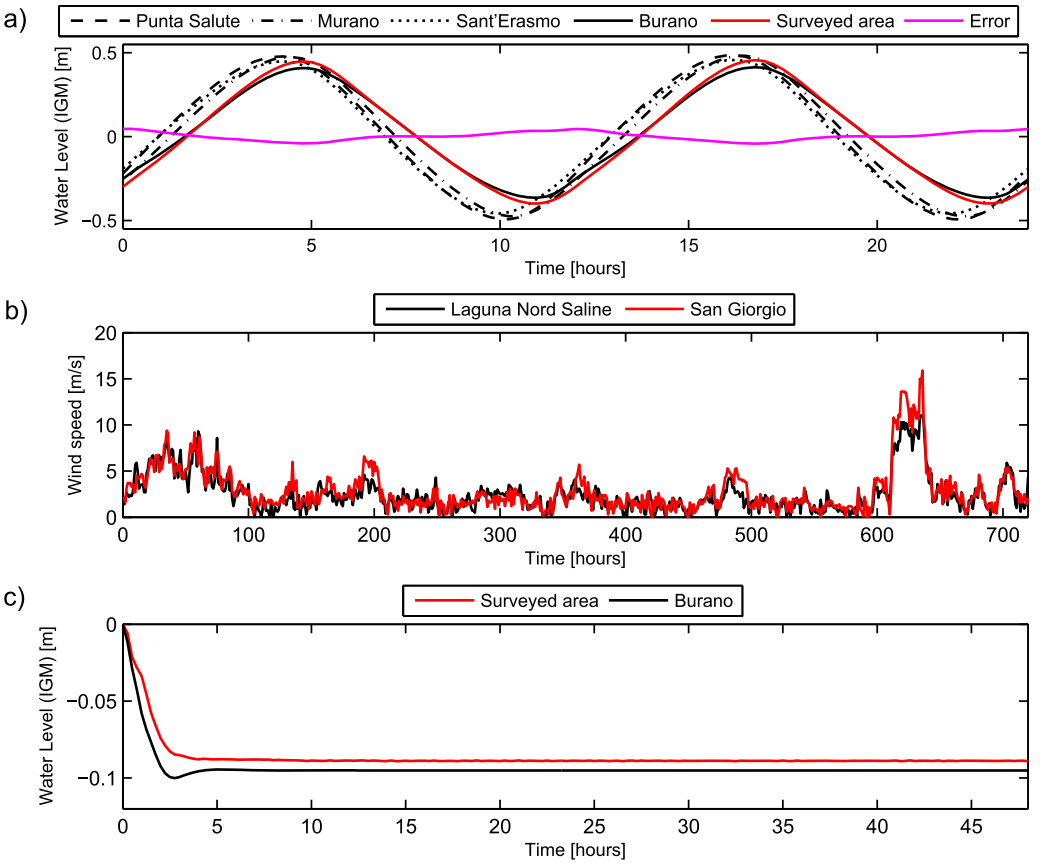


**Figure 6.** (a) Time evolution of water levels computed through a finite element numerical model solving the de Saint Venant Shallow Water equations [*Defina*, 2000; *Carniello et al.*, 2005]. Water levels are referred to the reference level IGM [*Genova*, 1942]. Each line represents the time evolution of the water level at a specific location: black dashed line, Punta Salute; black dash-dotted line, Murano; black dotted line, Sant'Erasmo; black line, Burano; and red line, surveyed area. Moreover, the magenta line represents the difference between the water level at Burano and nearby the monitored area. (b) Comparison between the time history of wind speed observed at Laguna Nord Saline (black line) and San Giorgio (red line) monitoring stations. (c) Comparison between computed water level setup induced by "Bora" wind at Burano (black line) and nearby the monitored area (red line).

Values of $\eta(t)$ are provided by Burano measurement station (Figure 1a). Even if the station is located at a distance of about 2.2 km from the monitored marsh, we assumed a quasi-steady propagation of the tidal wave [*Toffolon and Lanzoni*, 2010]. This assumption is supported not only by the relatively small distance between the two sites and the microtidal character of tide but also by the analysis of the flow field in the north part of the Lagoon of Venice by means of a numerical model solving the Shallow Water de Saint Venant equations, with particular attention to flooding and drying processes [*Defina*, 2000; *Carniello et al.*, 2005]. Figure 6a shows the temporal evolution of the water levels computed by assuming at the inlets of the lagoon a semidiurnal tide $\eta_{in}(t)=A/2\sin(\omega_{tide}t)+\Delta h_{MSL}$, with amplitude $A=1$ m, frequency $\omega_{tide}=1.45\times10^{-4}$ rad/s (equivalent to a period of 12 h) and mean sea level with respect to IGM reference [*Genova*, 1942] $\Delta h_{MSL}=0.065$ m. The simulated conditions are among the most critical in terms of water level difference between the Burano station and the monitored area. The considered tidal amplitude, in fact, is on average exceeded once a year. Nevertheless, the difference in water levels reaches maximum values of about 2–3 cm in correspondence of the crest and trough of the tidal wave, namely when the marsh is completely submerged or when the low water level prevents waves from reaching the marsh boundary. As a consequence, the error associated with the assumption of a quasi-steady propagation of the tidal wave does not affect significantly the estimate of wave height that promotes marsh erosion. Numerical results also show that the maximum magnitude of the tide-induced current is around 0.1 m/s for the area in front of sectors 2–4, whereas it reaches 0.7 m/s at the inlet of the channel close to sector 1. This latter value is quite similar to the depth-averaged velocity at ebb tide (0.5 m/s) obtained from in situ ADCP measurements (Figure 3).

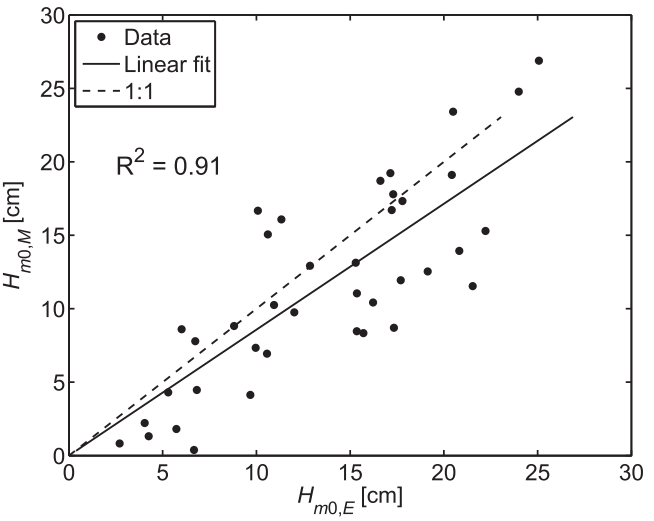


**Figure 7.** Relation between measured wave height $H_{m0,M}$ and estimated wave height $H_{m0,E}$. Black circles represent the scatterplot between $H_{m0,M}$ and $H_{m0,E}$. Black continuous line is the linear regression of $H_{m0,M}$ on $H_{m0,E}$. Black dashed line is the 1:1 line.

The wind velocities employed in equations (4) and (5) are those obtained by averaging the data collected at the monitoring stations of Laguna Nord Saline and San Giorgio (Figure 1a). The investigated marsh is in fact located between these two stations, along the direction of the "Bora" wind, and the two data sets almost overlap (Figure 6b), indeed a linear regression among them led to $R^2 = 0.82$.

Wind-induced setup may also influence the difference in water level at the investigated area and at the monitoring station of Burano where the water level is measured. To estimate this effect, a numerical simulation was carried out, in which water level in the lagoon is forced by a northeast wind of 12 m/s. Figure 6c shows that the maximum difference of the water levels between Burano and the monitored area is almost negligible, around 1 cm.

### 3.3. Relation Between $H_{m0,E}$ and $H_{m0,M}$

Relation between $H_{m0,M}$ and $H_{m0,E}$ was obtained through the calibration of relations (4) and (5). Since $H_{m0,M}$ has been obtained from measurements collected every 1.5 h while $H_{m0,E}$ is computed at intervals of 1.0 h, input data to equations (4) and (5) are linearly interpolated at the time instants corresponding to measured wave heights. Figure 7 shows the scatterplot of estimated and measured wave heights. Linear regression among data yields

$$H_{m0,M} = 0.87 H_{m0,E} \tag{7}$$

with a squared correlation coefficient $R^2 = 0.91$. The value of $f_c$ related to the measured wave height was in the range 1.0–2.5 Hz and the representative period associated with the storm surges was around 1.0–2.0 s. Relation (7) is then used in the following to determine the wave energy flux.

### 3.4. Erosion Rates

Erosion was measured from November 2013 to April 2015, roughly one survey per month, by means of 65 erosion pins placed horizontally at different heights along the bank scarp (vertically spaced about 0.4 m, see Figure 8) and at different position of the marsh shoreline (laterally spaced about 2 m).

Table 5 summarizes the number of pins employed per each sector. The erosion length, $L_{er}$ (Figure 8b), has been defined as the local retreat for each pin with respect to the previous survey. We set $L_{er} = 5.0 \times 10^{-3}$ m when the observed retreat length resulted in the range 0.0–1.0 $\times 10^{-2}$ m. Every time a mass failure occurred and the pin remained inserted in the slumped block, the eroded length was set equal to the width of the block. The pin was then reinserted in the marsh bank according to its original elevation. The positions of the bank top, bank toe, and pin elevation with respect to Punta Salute were determined through an electronic distance sensor (model Wild/Leica 2002, accuracy 1 mm + 1 ppm), after a datum point on the salt marsh was identified through GPS measurements.

The erosion rates, expressed in $m^2$/yr, were evaluated by considering a vertical section of the bank, containing at least one pin (Figure 8b). First, the eroded cross-sectional area is calculated as $L_{er,ji} \cdot L_p$ (black dashed portion in Figure 8), with $L_p$ the vertical extension of the slice of bank around a given pin over which the waves exert their erosive action. Next, the erosion rate is estimated by dividing the eroded area by the time interval $\Delta t$ during which erosion occurred, owing to the action of the waves striking the portion of the marsh bank associated with the considered pin. The $i$th pin located in the $j$th sector is potentially subject to erosion for a time span $\Delta t_{ji}$ determined through the relation:

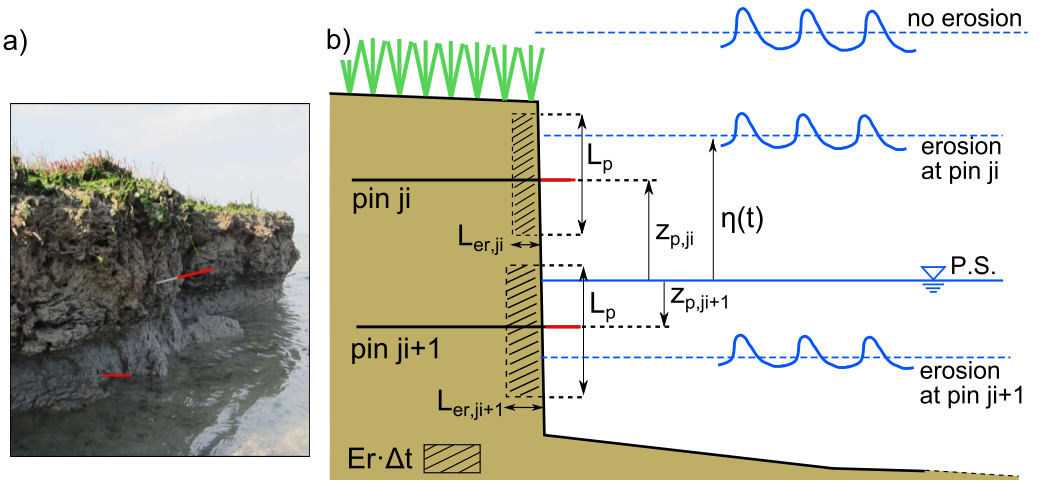


**Figure 8.** (a) View of two erosion pins located on the same vertical line for sector 1. (b) Sketch of the procedure employed to compute the eroded area and the erosion rates for the *j*th sector. $z_{p,ji}$ and $z_{p,ji+1}$ are the elevations of the pins *ji* and *ji* + 1 with respect to the reference level of Punta Salute (PS); $L_p$ is the bank thickness subject to erosion associated with each pin; $\eta$ is the water level with respect to Punta Salute; $L_{er,ji}$ and $L_{er,ji+1}$ are the erosion lengths measured at pins *ji* and *ji* + 1, respectively; and the black dashed area represents the volumetric erosion per unit length of the marsh boundary ($m^3/m$).

$$\Delta t_{ji} = \int_{\Delta T} g_{ji}^{\eta} \cdot g_j^{\theta} \cdot g^{P_w}\, d\tau \tag{8}$$

where $\Delta T$ is the time span between two consecutive surveys, and the generalized functions $g_{ji}^{\eta}$, $g_j^{\theta}$, $g^{P_w}$ work as switches that are activated when the pin is potentially subject to erosion. They are based on water level $\eta$, wave direction $\theta(=\theta_w)$, and wave power $P_w$, respectively. In particular,

$$g_{ji}^{\eta} = \begin{cases} 1 & \text{if } z_{p,ji} - L_p^{\text{down}} \le \eta(t) \le z_{p,ji} + L_p^{\text{up}} \\ 0 & \text{otherwise} \end{cases} \tag{9}$$

with $L_p = L_p^{\text{down}} + L_p^{\text{up}}$ and $L_p^{\text{down}} = L_p^{\text{up}} = 15$ cm;

$$g_j^{\theta} = \begin{cases} 1 & \text{if } \theta(t) \in \Delta\theta_j \\ 0 & \text{otherwise} \end{cases} \tag{10}$$

where $\Delta\theta_j$ is the range of wind directions potentially influencing the jth sector where the pin is located;

$$g^{P_w} = \begin{cases} 1 & P_w > 0 \\ 0 & \text{otherwise} \end{cases} \tag{11}$$

where Pw is the hourly wave energy flux (see section 3.4).

The erosion rate $Er_j$ ($m^2$/yr) associated with the *j*th sector is finally computed as

$$Er_j = \frac{1}{N_{p,j}} \sum_{i=1}^{N_{p,j}} \frac{24 \cdot 365}{\Delta t_{ji}} L_{er,ji} L_p \tag{12}$$

with $N_{p,j}$ the number of pins placed in the *j*th sector.

**Table 5.** Number of Deployed Pins Per Each Sector in Which the Marsh Edge Has Been Divided According to the Mean Edge Orientation and the Possible Influence of Boat-Induced Waves

| Sector 1 | Sector 1a | Sector 1b | Sector 2 | Sector 3 | Sector 4 |
|---|---|---|---|---|---|
| 18 | 3 | 3 | 7 | 14 | 20 |

### 3.5. Wave Energy Flux

Wave energy flux is determined by linear wave theory as

$$P_w = E \cdot c_p \cdot n \tag{13}$$

in which $E = \rho g H_{m0}^2/16$, $\rho$ is the water density, $c_p$ is the phase velocity,

$n = \frac{1}{2}\left[1 + \frac{2kh}{\sinh(2kh)}\right]$, and $H_{m0}$ is the wave height impinging the marsh bank, estimated on the basis of the functional relation (7).

Wave power $P_w$ is thus calculated hourly from the values of $H_{m0,E}$ and $T_p$, obtained by data provided by various measurement stations within the Lagoon of Venice (Figure 1a). The effective wave energy flux striking the $j$th sector for a specific interval of time $\Delta T$ is obtained from

$$P_{w,j} = \frac{1}{N_{p,j}} \sum_{i=1}^{N_{p,j}} \left[ \frac{1}{\Delta t_{ji}} \int_{\Delta T} P_w(\tau) \cos(\theta - \theta_{n,j}) \cdot g_{ji}^{\eta} \cdot g_j^{\theta} \cdot g^{P_w} \, d\tau \right] \tag{14}$$

with $\theta - \theta_n$ the angle that wind direction forms with the normal to the average orientation of the $j$th sector (note that sector 3 is considered to be divided into two parts with different orientations due to its nonuniformity along the marsh borderline).

### 3.6. Mathematical Model of Bank Edge Retreat

In order to interpret the effect of cantilever bank failure on the overall bank retreat, we developed a simplified model, taking into account vertical gradients in erosion rates due to both different soil erodibility and impinging wave energy flux. We assume a simple cross-shore profile as depicted in Figure 10. The bank, of height $b_h$, is divided in an upper and a lower layer, of thickness $\Delta L_{toe} = \Delta L_{top} = b_h/2$ and erodibility $r_{top}$ and $r_{toe}$, respectively, and an underneath shoaling profile starting at an elevation $d$ with respect to the adjacent mudflat. Only two layers with different erodibility are considered in order to maintain the model as simpler as possible. The bank is subject to continuous wave forcing modulated by the tide (approximate to a semidiurnal tide with period $T_{tide}$ equal to 12 h), and two different values of wave height are considered. The upper layer is eroded when the mean water surface elevation $\eta$ falls between $z_{b,avg}$ and $z_{b,avg} + \Delta L_{top}$, whereas the lower layer is eroded when water level falls between $z_{b,avg} - \Delta L_{toe}$ and $z_{b,avg}$, with $z_{b,avg}$ the elevation of the horizontal surface which separates the upper and the lower layer of the bank. Moreover, we denoted by $x_{top}$ and $x_{toe}$ the position of the upper and lower edge of the scarp in transverse direction, with $x_{avg} = \frac{1}{2}(x_{top} + x_{toe})$.

Wave energy flux Pw is computed through equation (13), assuming that the bank retreat is due only to wave impact. The cumulative retreats of the two portions of the bank are calculated as

$$x_{top}(t + \Delta t) = x_{top}(t) + \frac{r_{top} P_w \Delta t}{\Delta L_{top}} \tag{15a}$$

$$x_{toe}(t + \Delta t) = x_{toe}(t) + \frac{r_{toe} P_w \Delta t}{\Delta L_{toe}} \tag{15b}$$

Cantilever failure is assumed to occur when, during the simulation, $x_{top} - x_{toe}$ exceeds a given threshold $s_{max}$. Once mass failure occurs, the value of $x_{toe}$ is increased of 0.5 times the length of the failed block as proposed by *Gabet* [1998]. This assumption is made in order to consider that slumped blocks provide a certain protection to the bank toe before their relatively rapid removal by erosion.

## 4. Results

An overall view of the erosion processes acting on the investigated salt marsh is shown in Figure 11. The cumulative average retreat is plotted per each sector by either considering (Figure 11a) or excluding (Figure 11b) mass failures. The yearly retreat ranges from 18 to 80 cm/yr. Moreover, it clearly appears that sector 4 was subject to the highest retreat, which strongly increases when also mass failures are included (almost doubling).

Figure 12 shows the scatterplot of $P_{w,j}$ versus $Er_j$ for the various sectors in which the marsh edge has been subdivided, by either excluding or including mass failures from the analysis. In both cases, data sampled at too short (surveys 2 and 3) and too long (surveys 1 and 4) intervals of time are not considered (Table 3). Note that sectors 1a and 1b, owing to their peculiar morphology (see section 2), do not show a clear correlation between wave energy flux and erosion rate ($R^2$ equal to 0.1 and 0.22, respectively). Hence, the related scatterplots are not reported in Figure 12. The analysis carried out excluding mass failure events (Figure 12, black dots) indicates a relatively high correlation ($R^2 = 0.73$–$0.77$) for sectors 1–3, with a linear trend

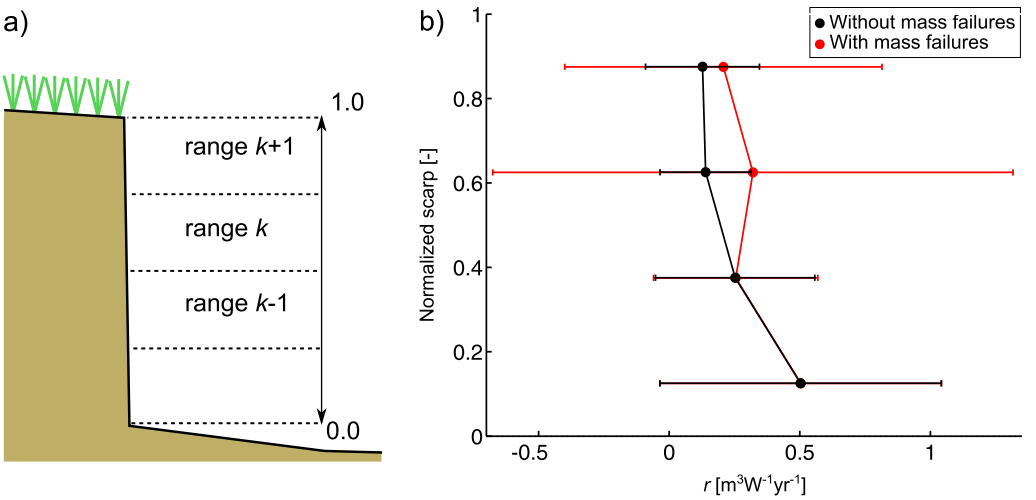


**Figure 9.** (a) Sketch of the framework employed to determine the average ratio $r$ of erosion rate to wave energy flux for pins located within the same elevation range along the scarp. (b) Plot of the $r$ averaged over sectors 1–4, by either considering (red dots) or excluding (black dots) mass failures. Error bars correspond to one standard deviation.

exhibiting different values of the slope and intercept with the $x$ axis. The lower correlation ($R^2 = 0.54$) for sector 4 (Figure 12d) is likely due to the high frequency of mass failures in this sector. Possibly, blocks slumped at the beginning of an observation interval (and hence not completely removed when the subsequent field survey was carried out) provided a defense for the bank against wave attack. Indeed, the values of the squared correlation coefficients, when mass failures are accounted for, are quite similar for sectors 1, 3, and 4. These lower values of $R^2$ can be explained by observing that mass failure is not immediately correlated to the wave energy flux at the time scale of months. In general, a time period characterized by intense wave forcing, preparing bank morphology to a mass failure, can be followed by a more calm period during which the failure occurs. A recognizable, although weak, linear trend, can be observed even including mass failures, provided their frequency is relatively high. In this case, slumping events tend to increase globally the erosion rates with respect to the case they are not accounted for (Figure 12d).

The existence of a threshold of the wave power for which erosion occurs is also identifiable in Figure 12 from the intercept of the regression lines with the horizontal axis. Considering the wave power averaged over a monthly time scale, this threshold ranges about 1–2 W/m, at least in three sectors.

The effect of wave attack at different levels along the scarp of the salt marsh edge is investigated in Figure 9. We compared the average of the ratios of erosion rates $Er_{ji}$ to wave energy flux $P_{w,ji}$ among groups of pins located at the same elevation range $k$ (Figure 9a) with respect to the bank toe. In particular, four different elevation ranges have been considered along the bank scarp normalized with its overall height (Figure 9a). The ratio $r_k$ for the $k$th range is determined as

$$r_k = \frac{1}{N_k} \sum_{i \in \text{range}(k)} \frac{Er_{ji}}{P_{w,ji}} \tag{16}$$

Figure 9b shows the values attained by the erodibility $r_k$ along the vertical profile of the bank by either considering or excluding mass failures. In general, $r_k$ tends to increase in the lower portion of the bank scarp, which results, on average, invariably more prone to erosion. Mass failure events, however, tend to increase $r_k$ also in the upper part of the bank, determining a higher standard deviation, as a consequence of the reduced correlation between wave energy flux and erosion rates discussed above.

The mathematical model describing the effect of cantilever failures on bank retreat (Figure 10) was run changing the ratio $r_{toe}/r_{top}$, and keeping fixed the other parameters, namely: $H_{rms} = 10, 20$ cm; $T = 1.5$ s; $A_{tide} = 1$ m; $T_{tide} = 12$ h; $b_h = 0.8$ m; $d = 0.4$ m; and $s_{max} = 0.55$ m (the width of observed slumped blocks falling in the range 0.25–0.7 m).

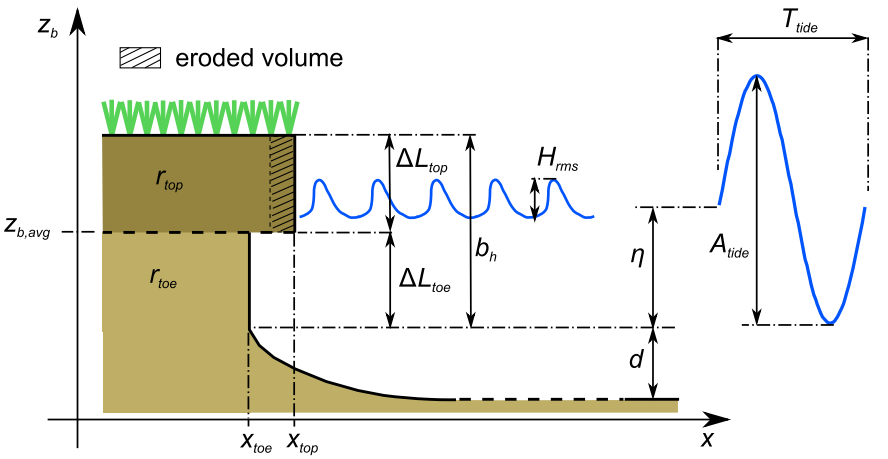


**Figure 10.** Sketch of the bank retreat model.

Figure 13 reports the ratio between the cumulative lateral retreat $x_{avg}$ and its equivalent value $x_{avg,eq}$, as a function of the ratio $r_{toe}/r_{top}$ computed after around 1460 tidal cycles (i.e., 2 years). The value of $x_{avg,eq}$ is obtained by running the model considering a uniform value for the scarp erodibility, equal to the average between $r_{top}$ and $r_{toe}$. Circles and crosses of different colors represent the output of the model in case $r_{toe}$

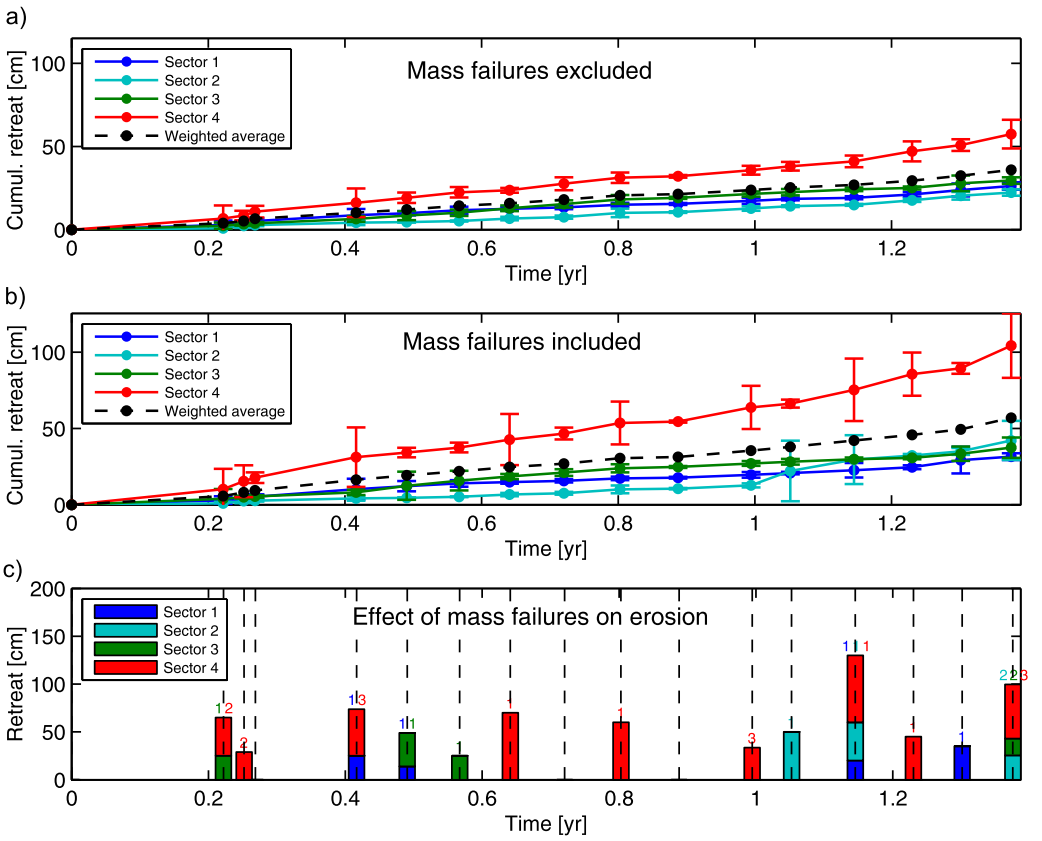


**Figure 11.** (a, b) Cumulative average retreat (in cm) observed in sectors 1–4 and average retreat weighted on the number of pins per each sector, by either (a) considering or (b) excluding mass failures. Error bars represent the standard deviation associated with the erosion calculated averaging the measurements over all the pins in a sector. (c) Horizontal retreat averaged over the number of mass failures only occurred during each interval. Colored numbers are the number of failures during an interval, associated with each sector. Black dotted vertical lines indicate the intervals.

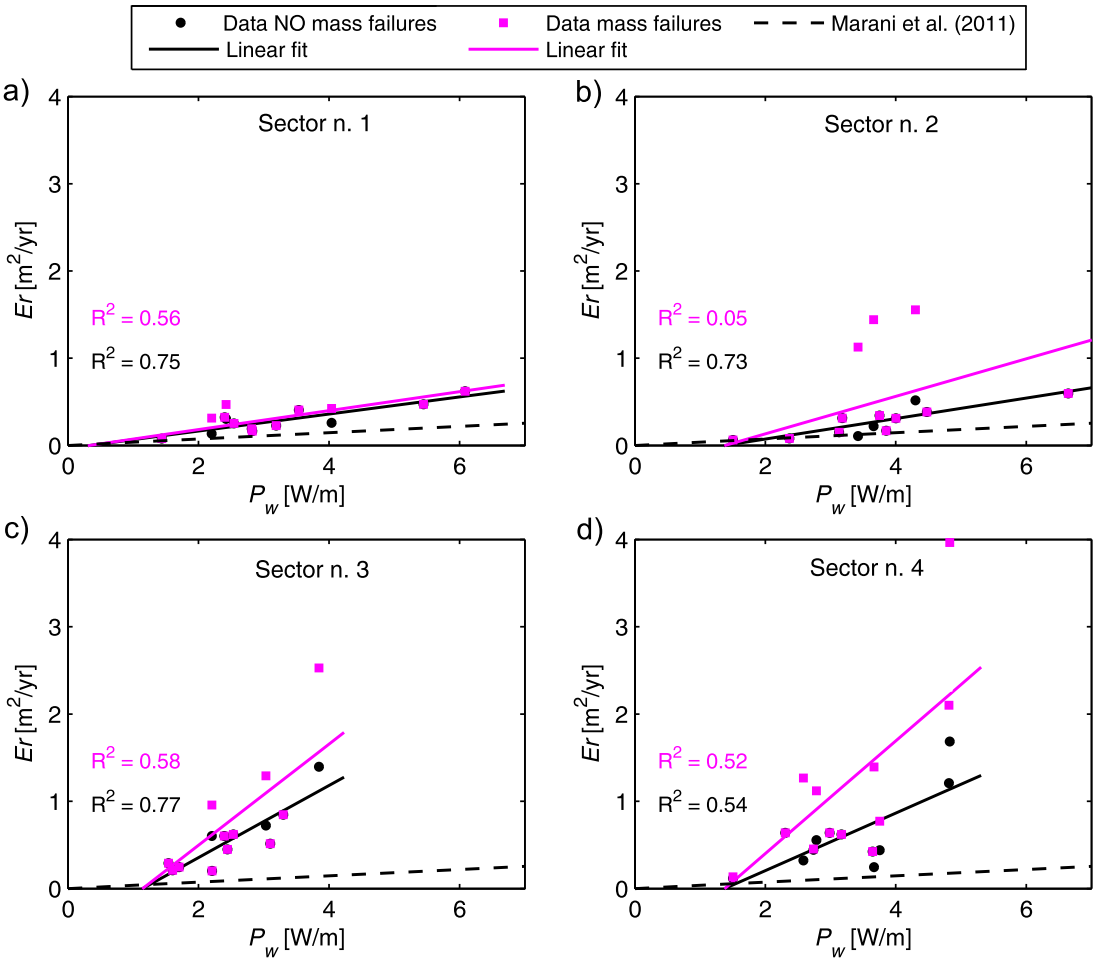


**Figure 12.** Scatterplots between wave energy flux, $P_w$, and erosion rate, $Er$, observed in sector 1–4 excluding (black dots) and including (magenta squares) mass failures in the erosion rates. Black and magenta continuous lines represent the linear regression among data, respectively, excluding or including mass failures. In each plot, the linear trend (slope 0.0364) proposed by *Marani et al*. [2011] is also reported (black dashed line). This trend has been reported on the basis of a global analysis of the marsh retreat within the Lagoon of Venice, carried out at the time scale of decades. The slopes of the various fitting lines are as follows: excluding mass failures, (a) 0.098, (b) 0.117, (c) 0.413, and (d) 0.330; including mass failures, (a) 0.108, (b) 0.225, (c) 0.577, and (d) 0.648.

and $r_{top}$ are referred to sectors 1, 2, and 4. Sector 3 was excluded from the analysis due to the limited number of erosion pins installed on the lower portion of the bank.

## 5. Discussion

The results of the analysis of the present field data are interpreted and discussed below with a specific focus on (i) the relationships between $P_w$ and $Er$ in each of the sectors; (ii) the time scales characterizing the physical processes; and (iii) the different erodibilities of the marsh scarp along the vertical direction.

As shown in Figure 12, only four of the six surveyed sectors (i.e., sectors 1–4) exhibited a relatively clear correlation between $P_w$ and $Er$. This result can be first explained by the few erosion pins (three) used to characterize the erosive trend in these sectors (1a and 1b). Indeed, the height of marsh banks in sectors 1a and 1b is really small (around 30–40 cm). Furthermore, the bathymetry of the tidal flat facing the salt marsh is characterized by really shallow depths up to a distance of 20–30 m from the salt marsh bank. The wave energy flux reaching the marsh edge, owing to the local influence of this shallow region, can be much smaller than the wave power determined from offshore bathymetric data used to compute (through equations (4) and (5)) wind waves characteristics. This difference between inshore and offshore bathymetry was partially affecting also the other salt marsh sectors, even though to a less extent. In addition, the orientation of the

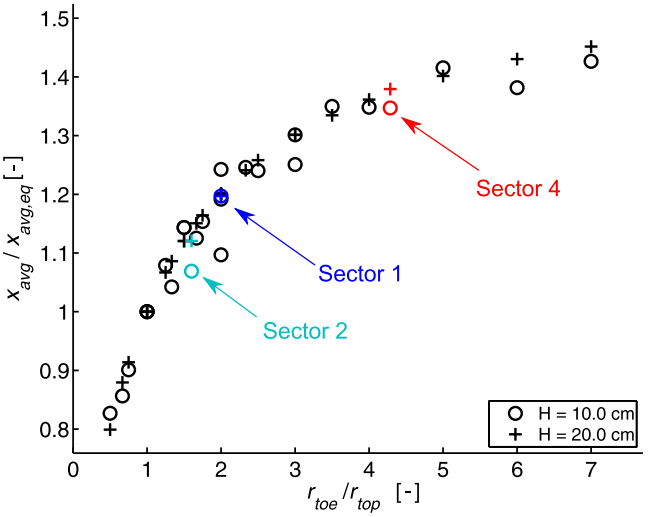


**Figure 13.** Ratio of the cumulative retreat $x_{avg}$ to the equivalent cumulative retreat $x_{avg,eq}$ as a function of the ratio $r_{toe}/r_{top}$, after 1460 tidal cycle as a function of the ratio $r_{toe}/r_{top}$ (black circles: $H_{rms}$ = 0.10 m; black crosses: $H_{rms}$ = 0.20 m). Colored markers are associated with values of $r_{top}$ and $r_{toe}$ of sector 1 (blue), sector 2 (light blue), and sector 4 (red).

boundary of sectors 1a and 1b makes them particularly protected and a restricted wind direction span can directly affects the marsh edge.

As already pointed out, sector 4 shows the lowest value of the squared correlation factor $R^2$. This result can be attributed to the high frequency of mass failures in this sector. Slumped blocks (with observed width in the range 0.25–0.7 m) may act as a defense barrier against wave attack before their complete removal, and as a consequence, high values of the wave energy flux may not be correlated to high erosion rates. We also noted that prediction of failure events is anyhow problematic when wave energy fluxes reaching the marsh edge are relatively low, is in the present case. Similar difficulties have been pointed out by *Leonardi and Fagherazzi* [2014] even in the case of salt marshes with larger fetches in front of them (Plum Island Sound, Massachusetts, and Virginia Coast Reserve, Virginia, USA) and, hence, subject to stronger wave energy fluxes.

We thus argue that the occurrence of many occasional mass failures is also responsible for the low correlation observed in sector 2 (Figure 12b), in case mass slumping is considered. On the other hand, a linear trend is recognizable for sectors 3 and 4, since mass failures were either not large (sector 3), or occurred almost once for each time interval between two consecutive surveys (sector 4, Figure 11c).

A possible explanation for the higher erosive trends exhibited by sectors 3 and 4, as compared to sectors 1 and 2, despite similar soil composition and vegetation cover, can be related to the presence of a shallower mudflat just in front of the latter two sectors. As a consequence, the wave power, estimated with a spatially averaged value of the offshore water depth in front of each sector, turns out to be slightly overestimated while, in reality, it is partially reduced as it reaches the bank. Furthermore, the effect of boat-induced waves might have played a role, since sectors 3 and 4 were potentially subject to wave forcing produced by the passage of boats traveling from Venice and Murano to Burano. Nevertheless, no quantitative information about the boat traffic was available and such aspect will be investigated in the future.

The data reported in Figures 12b–12d are characterized by values of the intercepts of regression lines with the abscissa in the range 1–2 W/m. This result suggests the existence of a threshold $P_{w,cr}$ for the onset of erosion due to wave impact having a value similar to that suggested by *Mariotti and Fagherazzi* [2010] (equal to 3 W/m). However, we cannot exclude that at lower time scales, the erosion threshold might be different due to the different averaging interval employed to determine the wave energy flux. In other words, the sampling interval can affect the estimated erosion rate, as well as it can influence the rate of sediment transport [*Singh et al.*, 2009]. The fact that sector 1 does not exhibit a clear erosion threshold (Figure 12a) may be explained by its location near the inlet of a deep tidal channel. Current induced shear stresses can thus induce particle by particle erosion even in the absence of surface waves as suggested by the values of tidal currents computed numerically and measured in the field (see section 3.2).

The effect of the time scale at which the erosion rates are analyzed emerges clearly by the comparison of present results (obtained considering a monthly time scale) with those obtained by *Marani et al.* [2011] (Figure 12) who analyzed data observed at intervals of a few decades. The main reason for the higher erosion rates emerging from the present data set is associated with the different time scales considered in the analyses. The erosion rates obtained by *Marani et al.* [2011] have been estimated by considering several sites in the Lagoon of Venice and comparing aerial photos acquired in 1970, 1995, and 2004. An average retreat was found by comparison, which was then multiplied by the bank height to recover a volumetric erosion per unit length ($m^3$/m). The time span

during which the erosion occurred, estimated excluding all periods in which the marsh was submerged, was of the order of decades. As a consequence of the larger time interval used to estimate the erosion rate, the mean speed of bank retreat turns out to be reduced. This result is not surprising and is similar to the dependence of the rate of bed load transport on sampling frequency described by *Singh et al.* [2009]. Longer time scale observations tend to smooth out higher peak fluctuations and include both variations intrinsic to the physical processes at work and possible changes in external forcing (due, e.g., to human activities or climate change). In order to build up reliable process based models for investigating possible long-term evolutionary scenarios, these latter effects should be avoided by carrying out field observations on short enough time scales, as those considered here.

Figure 9b might show that the lower portion of the marsh bank is more prone to erosion than the higher part. This behavior may have a twofold explanation. On the one hand, the presence of the root mat due to the vegetated cover can increase the resistance to erosion of the upper part of the bank [*Van Eerdt*, 1985; *Chen et al.*, 2012; *Tuan and Oumeraci*, 2012]. On the other hand, an increased forcing on bank scarp might result from the analysis of wave hydrodynamics. Let us assume, for the sake of simplicity, an equivalent wave energy flux impinging the top and the toe of the bank. This ideal case neglects the effect of lower average water depth, which reduces the wave height reaching the bank, all other things being equal. When the mean water level reaches the bank top, wave energy is partially reflected and wave breaking does not necessarily occur. Conversely, when the mean water level is around the lower part of the bank scarp, waves generally break before impacting the bank, leading to a higher turbulence intensity and negligible wave reflection. Consequently, the erosive power of the waves is much larger with respect to that characterizing the partially reflective wave pattern occurring for higher mean water levels. This possible explanation of the higher erosion rate exhibited by the bank scarp is further supported by the small variability of soil composition (Figure 4) along the vertical profile. In summary, both the binding effect of roots and the local characteristics of the wave field are likely responsible for the greater erodibility of the scarp toe and promote cantilever mass failures.

The results of the simulations run with the mathematical model (Figure 10) described in section 3.6 show that increasing the difference of erodibility along the scarp of the salt marsh leads to an increase of cumulative lateral retreat with respect to the equivalent case of uniform erodibility (Figure 13). The process of cantilever formation and subsequent failure may increase roughly up to 50% the cumulative lateral retreat, provided that the simulation lasts the time necessary for mass failure events to occur. The larger scatter resulting for $H = 10$ cm, can be ascribed to the fact that during the simulated time interval (2 years), less mass failures occurred. In particular, those banks with larger values of the ratio $r_{toe}/r_{top}$, display a greater retreat since mass failures may occur more often. Also, the model suggests that those banks with a relative less erodible toe layer ($r_{toe}/r_{top} < 1$) display a reduction in the lateral retreat.

The results of the model can partly explain why sector 4 experienced a higher cumulative retreat with respect to the others. Even if the average erodibility (i.e., the ratio between erosion rate and wave power) of sector 4 is higher than sectors 1 and 2, this effect is emphasized due to a higher ratio $r_{toe}$ to $r_{top}$.

In addition, groundwater flow may indirectly influence mass failures promoting stress variation inside the solid phase [*Cola et al.*, 2008], possibly leading to the formation of tension cracks. However, this aspect is not investigate here and will be accounted for in future research.

Present finding has several implications on the lateral evolution of salt marshes. The presence on the marsh edge of a vegetated top layer of soil, with increased overall cohesion via the root system, and of a relatively more erodible toe layer, lead to higher retreats due to mass erosion (in the present case through cantilever failures). This suggests that vegetation does not necessarily guarantee the lateral stability of salt marshes. Indeed, while vegetation can have a positive role to locally decrease the proneness to erosion [*Howes et al.*, 2010; *Chen et al.*, 2012; *Tuan and Oumeraci*, 2012], present results suggest that vegetation by itself may be not sufficient to ensure, globally, a reduction of lateral erosion. As pointed out by *Mariotti and Fagherazzi* [2013], lateral dynamics is in general driven by sediment transport processes and vertical evolution of the adjacent tidal flats, but a significant role can be also played by the retreat mechanism occurring at local scale.

## 6. Conclusions

Field measurements have been carried out in a salt marsh located in the northern part of the Venice Lagoon in order to investigate the effects of wind waves on the retreat mechanism of the marsh edge and a simple

mathematical model to interpret field data has been developed. Wave height measurements coupled with inshore wave climate estimates based on offshore wind, fetch, and depth data were employed to relate the wave forcing at the monitored marsh to the bank erosion rate.

Global average retreat rates, reaching up to 80 cm/yr, are usually different along the marsh borderline due to different wind exposure, local bathymetric features, and localized dynamics controlled by the nonuniform erodibility of the scarp. The effect of repeated mass failures can almost double the average retreat rate for a specific sector.

A clear linear correlation between wave energy flux and erosion rate, at short (monthly) temporal scales, can be found when mass failure events are excluded from the analysis. Including mass failure events leads to a linear correlation only if episodes of mass collapse are frequent. In general, the slumping of unstable blocks is not necessarily correlated to the instantaneous wave forcing. An unstable bank configuration is usually enhanced by wave attack, but the final mass failure may occur later on, also during a more calm period.

The ratio of wave power to erosion rate is generally higher than those obtained in other studies averaging lateral retreat data over much larger time intervals (of the order of decades). The problem associated with the choice of a suitable sampling time turns out to be similar to that emerging in bed load transport, whereby mean sediment transport appears to be dependent on the sampling time.

The formation of cantilever profiles, generally present in the field, can be explained by the higher propensity to erosion of the lower part of the bank scarp with respect to the top. This result is likely due to the presence of the root mat in the upper bank portion as well as to the local characteristics of the flow field.

A simple mathematical model, based on the differential erodibility of the salt marsh scarp, showed that the presence of a less resistant toe layer leads to higher cumulative retreat, as compared to the equivalent case in which erodibility is uniformly distributed along the vertical profile. This finding reveals that the presence of vegetation does not necessarily ensure the reduction of the lateral retreat of a salt marsh, even if it reinforces the soil against erosion. A stronger top layer might in fact promote the formation of cantilever profiles, which in turn, lead to more frequent mass failure events, thus globally increasing the lateral retreat.

Future developments should address the effects of a single storm surge on bank morphology through surveys carried out immediately before and after a strong storm event.

The role of boat-induced waves should be quantified, so that its relative contribution to the erosion rate can be considered.

This notwithstanding, the present findings are useful not only for prediction purposes but also for developing and validating bank erosion models.

**Acknowledgments**
Chiara Pistoresi, Simone Bonistalli, Laura Nardi, Enrica Belluco, Marco Giada, and Daniele Steffinlongo are gratefully acknowledged for their work during the field measurements campaign. This work has been supported by the University of Padua through the Athenaeum Project "Morphodynamics of marsh systems subject to natural forcing and climate changes" and by the University of Florence through the Athenaeum Project "Morphodynamic evolution of salt marshes in tidal environments." All the data used in the paper are available by contacting the corresponding author.

## References

Barbier, E. B., S. D. Hacker, E. W. Koch, A. C. Stier, and B. R. Silliman (2011), The value of estuarine and coastal ecosystem services, *Ecol. Monogr.*, *81*(2), 169–193.

Bendoni, M., S. Francalanci, L. Cappietti, and L. Solari (2014), On salt marsh retreat: Experiments and modeling toppling failures induced by wind waves, *J. Geophys. Res. Earth Surf.*, *119*, 603–620, doi:10.1002/2013JF002967.

Bird, P. A. D. (1993), Measurement and analysis of sea waves near a reflective structure, PhD thesis, Sch. of Civ. and Struct. Eng., Univ. of Plymouth, Plymouth, U. K.

Bishop, C. T., and M. A. Donelan (1987), Measuring waves with pressure transducers, *Coastal Eng.*, *11*, 309–328.

Breugem, W. A., and L. H. Holthuijsen (2007), Generalized shallow water wave growth from Lake George, *J. Waterw. Port Coastal Ocean Eng.*, *133*, 173–182.

Callaghan, D. P., T. J. Bouma, P. Klaassen, D. Van der Wal, M. J. F. Stive, and P. M. J. Herman (2010), Hydrodynamic forcing on salt-marsh development: Distinguishing the relative importance of waves and tidal flows, *Estuarine Coastal Shelf Sci.*, *89*, 73–88.

Carniello, L., A. Defina, S. Fagherazzi, and L. D'Alpaos (2005), A combined wind wave-tidal model for the Venice lagoon, Italy, *J. Geophys. Res.*, *110*, F04007, doi:10.1029/2004JF000232.

Cavaleri, L. (1980), Wave measurement using pressure transducer, *Oceanol. Acta*, *3*, 339–346.

Chen, Y., C. E. L. Thompson, and M. B. Collins (2012), Saltmarsh creek bank stability: Biostabilization and consolidation with depth, *Cont. Shelf Res.*, *35*, 64–74.

Cola, S., L. Sanavia, P. Simonini, and B. Schrefler (2008), Coupled thermohydromechanical analysis of Venice lagoon salt marshes, *Water Resour. Res.*, *44*, W00C05, doi:10.1029/2007WR006570.

Cooley, J. W., and J. W. Tukey (1965), An algorithm for the machine computation of the complex Fourier series, *Math. Comput.*, *19*, 297–301.

Day, J. W., Jr., F. Scarton, A. Rismondo, and D. Are (1998), Rapid deterioration of a salt marsh in Venice Lagoon, Italy, *J. Coastal Res.*, *14*(2), 583–590.

Day, J. W., Jr., et al. (2007), Restoration of the Mississippi Delta: Lessons from hurricanes Katrina and Rita, *Science*, *315*(5819), 1679–1684.

Dean, R. G., and R. A. Darlymple (1991), *Water Wave Mechanics for Engineers and Scientists, Adv. Ser. Ocean Eng.*, vol. 2, 353 pp., World Sci. Publ. Co., River Edge, N. J.
Defina, A. (2000), Two-dimensional shallow flow equations for partially dry areas, *Water Resour. Res.*, *36*(11), 3251–3264.
Fagherazzi, S., G. Mariotti, P. Wiberg, and K. McGlathery (2013), Marsh collapse does not require sea level rise, *Oceanography*, *26*(3), 70–77.
Feagin, R. A., S. M. Lozada-Bernard, T. M. Ravens, I. Moller, K. M. Yeager, and A. H. Baird (2009), Does vegetation prevent wave erosion of salt marsh edges?, *Proc. Natl. Acad. Sci. U. S. A.*, *106*, 10,109–10,113.
Francalanci, S., M. Bendoni, M. Rinaldi, and L. Solari (2013), Ecomorphodynamic evolution of salt marshes: Experimental observations of bank retreat processes, *Geomorphology*, *195*, 53–65, doi:10.1016/j.geomorph.2013.04.026.
French, J. (2006), Tidal marsh sedimentation and resilience to environmental change: Exploratory modelling of tidal, sea-level and sediment supply forcing in predominantly allochthonous systems, *Mar. Geol.*, *235*(1), 119–136.
Gabet, E. J. (1998), Lateral migration and bank erosion in a saltmarsh tidal channel in San Francisco Bay, California, *Estuaries*, *21*(4B), 745–753.
Gedan, K. B., B. R. Silliman, and M. D. Bertness (2009), Centuries of human-driven change in salt marsh ecosystems, *Annu. Rev. Mar. Sci.*, *1*, 117–141.
Genova, (1942). [Available at http://www.igmi.org/.]
Houser, C. (2010), Relative importance of vessel-generated and wind waves to salt marsh erosion in a restricted fetch environment, *J. Coastal Res.*, *26*(2), 230–240.
Howes, N. C., D. M. Fitzgerald, Z. J. Huges, I. Y. Georgiou, M. A. Kulp, M. D. Miner, J. M. Smith, and J. A. Barras (2010), Hurricane-induced failure of low salinity wetlands, *Proc. Natl. Acad. Sci. U. S. A.*, *107*(32), 14,014–14,019.
Jadhav, R. S., Q. Chen, and J. M. Smith (2013), Spectral distribution of wave energy dissipation by salt marsh vegetation, *Coastal Eng.*, *77*, 99–107.
Jones, N. L., and S. G. Monismith (2007), Measuring short-period wind waves in a tidally forced environment with a subsurface pressure gauge, *Limnol. Oceanogr. Methods*, *5*, 317–327.
Kirwan, M. L., G. R. Guntenspergen, A. D'Alpaos, J. T. Morris, S. M. Mudd, and S. Temmermann (2010), Limits on the adaptability of coastal marshes to rising sea level, *Geophys. Res. Lett.*, *37*, L23401, doi:10.1029/2010GL045489.
Lee, D.-Y., and H. Wang (1984), Measurements of surface waves from subsurface gage, in *Proceedings of the 19th Coastal Engineering Conference*, pp. 270–286, Huston, Idaho.
Leonardi, N., and S. Fagherazzi (2014), How waves shape salt marshes, *Geology*, *42*(10), 887, doi:10.1130/G35751.1.
Marani, M., A. D'Alpaos, S. Lanzoni, and M. Santalucia (2011), Understanding and predicting wave erosion of marsh edge, *Geophys. Res. Lett.*, *38*, L21401, doi:10.1029/2011GL048995.
Mariotti, G., and S. Fagherazzi (2010), A numerical model for the coupled long-term evolution of salt marshes and tidal flats, *J. Geophys. Res. Earth Surf.*, *115*, F01004, doi:10.1029/2009JF001326.
Mariotti, G., and S. Fagherazzi (2013), Critical width of tidal flats triggers marsh collapse in the absence of sea-level rise, *Proc. Natl. Acad. Sci. U. S. A.*, *110*(14), 5353–5356.
McLoughlin, S. M., P. L. Wiberg, I. Safak, and K. J. Karen (2014), Rates and forcing of marsh edge erosion in a shallow coastal bay, *Estuaries Coasts*, *38*(2), 620–638.
Moller, L. (1999), Wave transformation over a salt marsh: A field and a numerical modeling study from North Norfolk, England, *Estuarine Coastal Shelf Sci.*, *49*, 411–426.
Moller, L. (2006), Quantifying saltmarsh vegetation and its effect on wave height dissipation: Results from a UK East coast saltmarsh, *Estuarine Coastal Shelf Sci.*, *69*, 337–351.
Poulain, P.-M., and F. Raicich (2007), Forcings, in *Physical Oceanography of the Adriatic Sea: Past, Present and Future*, edited by B. Cushman-Roisin et al., pp. 45–65, Springer, N. Y.
Priestas, A. M., and S. Fagherazzi (2011), Morphology and hydrodynamics of wave-cut gullies, *Geomorphology*, *131*(1–2), 1–13, doi:10.1016/j.geomorph.2011.04.004.
Ravens, M. T., R. C. Thomas, K. A. Roberts, and P. H. Santschi (2009), Causes of salt marsh erosion in Galveston Bay, Texas, *J. Coastal Res.*, *25*(2), 265–272.
Saville, T. (1954), The effect of fetch width on wave generation, *Tech. Memorandum 70*, Beach Erosion Board, Washington, D. C.
Schwimmer, M. M. (2001), Rates and processes of marsh shoreline in Rehoboth Bay, Delaware, USA, *J. Coastal Res.*, *17*(3), 672–683.
Seminara, G., S. Lanzoni, G. Cecconi (2011), Coastal wetlands at risk: Learning from Venice and New Orleans, *Ecohydrol. Hydrobiol.*, *11*(3–4), 183–202.
Silliman, B. R., J. Van de Koppel, M. W. McCoy, J. Diller, G. N. Kasozi, K. Earl, P. N. Adams, and A. R. Zimmerman (2012), Degradation and resilience in Louisiana salt marshes after the BP–Deepwater Horizon oil spill, *Proc. Natl. Acad. Sci. U. S. A.*, *109*(28), 11,234–11,239.
Singh, A., K. Fienberg, D. J. Jerolmack, J. Marr, and E. Foufoula-Georgiou (2009), Experimental evidence for statistical scaling and intermittency in sediment transport rates, *J. Geophys. Res.*, *114*, F01025, doi:10.1029/2007JF000963.
Temmerman, S., P. Meire, T. J. Bouma, P. M. J. Herman, Y. Tom, and H. J. De Vriend (2013), Ecosystem-based coastal defence in the face of global change, *Nature*, *504*(7478), 79–83.
Toffolon, M., and S. Lanzoni (2010), Morphological equilibrium of short channels dissecting the tidal flats of coastal lagoons, *J. Geophys. Res.*, *115*, F04036, doi:10.1029/2010JF001673.
Tuan, T. Q., and H. Oumeraci (2012), Numerical modeling of wave overtopping-induced erosion of grassed inner sea-dike slopes, *Nat. Hazards*, *63*, 417–447.
Tucker, M. J., and W. G. Pitt (2001), *Waves in Ocean Engineering, Elsevier Ocean Eng. Book Ser.*, vol. 5, 521 pp., Elsevier, Oxford, U. K.
Van der Wal, D., A. Wielemaker-Van den Dool, and P. M. J. Herman (2008), Spatial patterns, rates and mechanisms of saltmarsh cycles (Westerschelde, The Netherlands), *Estuarine Coastal Shelf Sci.*, *32*, 1247–1259.
Van Eerdt, R. R. (1985), Salt marsh cliff stability in the Oesterschelde, The Netherlands, *Earth Surf. Processes Landforms*, *10*, 95–106.
Welch, P. D. (1967), The use of the Fast Fourier Transform for the estimation of power spectra: A method based on time averaging over short modified periodograms, *IEEE Trans. Audio Electroacoust., AU-15*, 70–73, Southampton, U. K.
Wolf, J. (1997), The analysis of bottom pressure and current data for waves, paper presented at the 7th International Conference on Electronic Engineering in Oceanography, Conference Publication No. 49, Inst. of Electron. Eng., 23–25 June.
Young, I. R., and L. A. Verhagen (1996), The growth of fetch limited waves in water of finite depth. Part 1. Total energy and peak frequency, *Coastal Eng.*, *29*, 47–78.